

Embedded Ring Modulators and Switches

Das U^{1*} and Sadasivan V²

¹Department of Electrical Engineering, Indian Institute of Technology, Kanpur, 208016, Uttar Pradesh, India

²Central Electronics Engineering Research Institute (CEERI), Pilani, Rajasthan, India

Abstract

Micro embedded ring resonator electro-optic switching in InGaAsP based quantum well structures is briefly reviewed and all optic switching is presented. A 20Gbps electro-optic modulator with >12dB extinction ratio has been proposed using quantum confined stark effect tuning, for which a novel high speed coplanar-microstrip inverted ground plane transition has also been designed. All optical tuning is used to theoretically demonstrate a 20G packets/s switching with a 5dB switching ratio. The fabricated micro embedded ring resonator ring using e-beam lithography and Al lift off mask has been demonstrated and the measured device spectrum is found to match well with the simulated results.

Keywords: Electro-optic switch; All-optical switch; Embedded ring; InGaAsP

Introduction

Ring resonators are compact resonant filters which have applications in filtering [1], modulation [2], and switching [3]. Embedded rings have shown interesting spectral features and enhanced modulation response, for free carrier plasma tuning in Si [4]. Common tuning methods employed in semiconductor resonators include temperature [5], Franz-Keldysh (FK) effect in bulk semiconductors, carrier injection and quantum confined stark effect (QCSE) [6] in multi quantum wells (MQW). Temperature tuning is speed limited to ~1 MHz only and for free carrier based devices are constrained by large insertion losses and slow carrier transit times. Electro-optic tuning of rings has the advantage of fast compact integrated optic modulators for communication applications. On the other hand, all optical signal processing and switching has potential applications [3] in large and compact optical switching arrays without the electronic carrier induced delay. Hence, this study presents an electro-optic and an all-optical path switching embedded ring device for fast modulator or switching applications. In addition to the theoretical studies, a brief report of fabricated passive embedded ring device is also reported.

Electro-Optic Switch

QCSE tuning in MQW waveguides

An externally applied electric field results in change of absorption and refractive index in semiconductors due to change of bandgap and distortion of the wave function solutions of the bulk (FK) and QW (QCSE). For refractive index calculation of 10⁻⁵ precision (required for the embedded ring problem) using a detailed variation calculation for all energies [7] is prohibitively slow. Hence, usage of Kramers-Kronig integral over hundred inter-band transitions have been implemented here to obtain the required refractive indices.

The overall electro-optic change of effective index of a waveguide due to large applied external field 'E' is given ref. [6]

$$\Delta n_{eff} \approx \frac{1}{2} \Gamma_{bulk} n_{0,bulk}^3 \{r_{bulk} E + S_{bulk} (E^2 + 2EE_0)\} + \frac{1}{2} \Gamma_{QW} n_{0,QW}^3 (r_{QW} E + S_{QW} E^2) \quad (1)$$

Here the confinement factor Γ_i is obtained by electromagnetic field solution of bent and straight waveguide segments using a transfer matrix method, in addition to Bessel's equation solutions and the effective index method [7]; $n_{0,bulk}$ and $n_{0,QW}$ are the zero field refractive indices of bulk semiconductor and QW, respectively; r and s are the

linear quadratic electro-optic coefficients, with subscripts indicating the region. The effect of electro optic coefficients of bulk is ignored due to relatively small confinement in undoped bulk regions and large detuning from bulk band edge. Hence for high electric fields eqn. (1) can be approximated [8].

$$\Delta n_{eff} \approx \frac{1}{2} \Gamma_{QW} n_{0,QW}^3 (r_{QW} E + S_{QW} E^2) \quad (2)$$

Modeling of the embedded ring modulator

The modeling of the embedded ring resonator is done in a hierarchical manner. This method allows individual components like material, waveguides, couplers and rings to be modeled in a scalable manner from component to the system level. The static and dynamic models of the embedded rings used to study the output spectrum and the electro-optic modulation response have already been reported in detail [7].

The electrode design

The high speed contact for the ring resonator has been designed using a coplanar-to-microstrip transition section, as shown in Figure 1a. The microwave model has been simulated using a 'CST' software package. The coplanar line 75 μ m central conductor to ground line separation is 30 μ m. The width of microstrip regions is 4 μ m and the transition from coplanar end to microstrip is 200 μ m long. The coplanar lines are of 50 Ω impedance with a matched 50 Ω termination at the output port. The metal lines are considered to be ohmic on P⁺ and N⁺ InP. The isolation has been taken as silica although; a low loss polymer/air-bridge may be used immediately near the device. The microwave losses in doped substrates are expected to be very high, hence the bottom contact layer is assumed to be completely etched down to the semi-insulating (SI) substrate, outside the device region. The upper and lower contact layers of the ring has been modeled using

***Corresponding author:** Das U, Department of Electrical Engineering, Indian Institute of Technology, Kalyanpur, Kanpur, 208016, Uttar Pradesh, India, Tel: 0512 259 0151; E-mail: utpal@iitk.ac.in

Received June 16, 2017; **Accepted** June 25, 2017; **Published** June 30, 2017

Citation: Das U, Sadasivan V (2017) Embedded Ring Modulators and Switches. J Laser Opt Photonics 4: 163. doi: [10.4172/2469-410X.1000163](https://doi.org/10.4172/2469-410X.1000163)

Copyright: © 2017 Das U, et al. This is an open-access article distributed under the terms of the Creative Commons Attribution License, which permits unrestricted use, distribution, and reproduction in any medium, provided the original author and source are credited.

its conductivity obtained from doping dependent mobility values [9] and the intrinsic MQW region is approximated using the loss tangent of intrinsic InP [10].

As shown in Figure 1a, the yellow regions on the two sides are gold top contacts which act as the coplanar ground plane. This electrode tapers and reaches over the ring to constitute the microstrip ground plane, with the microstrip going underneath. For simplicity of the model, a single ring has been used during the microwave simulation. The bottom contact is made on a ridge of N⁺ layer. The N⁺ layer of the ring acts as the microstrip inside the ring. The most challenging part of this design has been to pass the microwave signal through the doped bottom contact part of the ring without incurring large loss. Since the conductivity (σ) of heavily doped semiconductors is ~100 times smaller than that of metals, using them as microstrips has not been very effective, although is necessitated by the device geometry. The $1 \times 10^{18} \text{cm}^{-3}$ doped N⁺ InP layer has a mobility which is ~5 times smaller than that of InGaAsP of the same doping, as indicated in Table 1. Hence an additional 30 nm thick InGaAsP layer has been included below the InP contact layer to provide electrical path, without significantly modifying the optical mode profile, and is used for the microwave simulation. This layer is deemed sufficient since the skin depths (δ_s) are <12 nm in the 10-40 GHz band. Even then the microstrip section made up of semiconductor dielectric accounts for ~96% of the total losses, which is ~40% of the incident microwave power. The total microwave insertion loss of the structure has been calculated to be 4dB with N⁺ InGaAsP as the bottom contact layer and 11dB with N⁺ InP as the bottom contact layer, respectively. The S-parameters of the structure is shown in Figure 1b. The computed 3dB bandwidth is 42 GHz with N⁺ InGaAsP as the bottom contact layer and 37GHz with N⁺ InP as the bottom contact layer.

The modulation process

The layer structure has P⁺-InGaAs (50 nm) top contact layer, followed by a P⁺-InP (200 nm), a P-InP (300 nm), an I-InGaAsP (10 nm), an I-MQW (470 nm), an I-InGaAsP (10 nm), an N-InP (200 nm), an N⁺-InP (2 μm) over a SI-InP (substrate) [7]. Twenty-three In_{0.65}Ga_{0.37}As_{0.80}P_{0.20} (10 nm) wells and twenty-four InP (10 nm) barriers have been used for the MQW layer (band gap of 1417 nm). The calculated MQW quadratic and the linear electro-optic coefficients at 1550 nm are $s_{QW}=3.85 \times 10^{-15} \text{cm}^2/\text{V}^2$ and $r_{QW}=-2.1 \times 10^{-10} \text{cm}/\text{V}$, respectively, which are close those given [6,8] for similar epitaxial structures. With I-InGaAsP (1.05 eV band gap) on top and bottom of MQW layer, the total I region thickness is 490 nm. An effective index

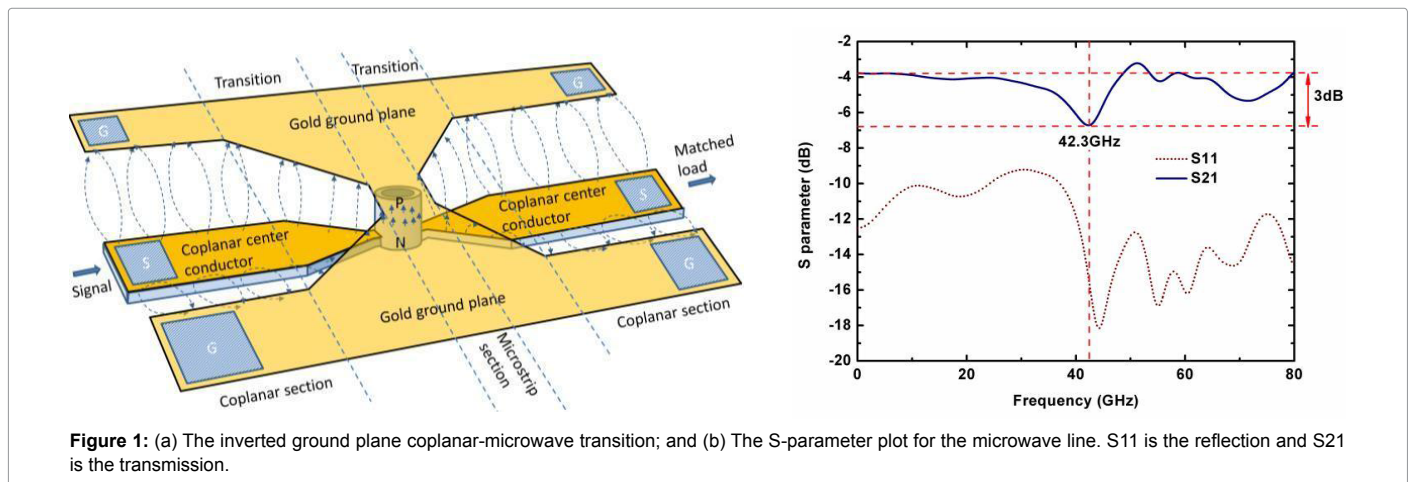
tuning of 2.4×10^{-4} is calculated for a 100 kVcm^{-1} applied field (~7V driving bias voltage) at 1550 nm. Internal 0 V field of 21 kV/cm was assumed. Due to proximity of the absorption peak, the calculated QW loss is thus obtained as 25 dB/cm and the free carrier loss in doped layers is calculated to be 13 dB/cm [11].

The embedded ring structure used in this study has a 5 μm outer and a 4.45 μm inner ring radius. The outer ring has a 2.1 μm straight waveguide segment, where it couples with the inner ring. The straight waveguide segments are 450 nm wide and tapers down to 200 nm in the middle of the coupler. The coupling gap is 100 nm and the coupling coefficient is ~20%, being aided by the taper. The ridge waveguides are etched >2 μm deep for reducing substrate leakage. The embedded ring

Simulation parameter	Value
Dimensions	
Broad width of coplanar centre line	150 μm
Coplanar centre line to ground gap	30 μm
Narrow width of microstrip	4 μm
Transition length	200 μm
Ring radius	5 μm
Ring core thickness	200 nm
Ring upper contact layer thickness	0.9 μm
Ring lower contact layer thickness	0.9 μm
Metal line thickness	400 nm
Ionized carrier concentration	
Intrinsic (MQW~InP) [10]	$6.70 \times 10^{15} \text{cm}^{-3} (\epsilon_{rs}=12.56, \tan\delta\sim 0.1)$
P+ – contact layer (InGaAs) [9]	$1 \times 10^{19} \text{cm}^{-3} (\epsilon_{rs}=13.9, \sigma\sim 69183 \text{S/m})$
N+ – contact layer (InP) [9]	$1 \times 10^{18} \text{cm}^{-3} (\epsilon_{rs}=12.56, \sigma\sim 41120 \text{S/m}, \delta_s=30 \text{nm}@10 \text{GHz})$
N+ –contact layer (InGaAsP, λ=1060 nm) [9]	$1 \times 10^{16} \text{cm}^{-3} (\epsilon_{rs}=13, \sigma\sim 220585 \text{S/m}, \delta_s=12 \text{nm}@10 \text{GHz})$
Semi insulating (Fe doped, InP substrate) [11]	$(\epsilon_{rs}=12.56, \tan\delta\sim 6.6 \times 10^{-4})$
Simulation settings	
Simulation frequency range	0-80 GHz
Simulated microwave power	0.5 W
Total simulation region	$106 \mu\text{m} \times 6010 \mu\text{m} \times 1060 \mu\text{m}$
Region boundary	$E_t=0$
Port	Waveguide port
Solver used	Time domain
Smallest mesh size	195 nm

δ_s is the skin depth and σ is the conductivity.

Table 1: Comparison of embedded ring all-optical switch with other reported devices.



spectrum and its QCSE tuning are shown in Figure 2. This spectrum shows sharper roll off on the blue end of the spectrum and is caused by odd number difference between the inner and outer ring resonance peak numbers [4]. When the externally applied electric field is low (0V bias) a continuous wave laser source of 1542.61 nm at the “input port” gets blocked from exiting the “through port” whereas when the electric field is high (7 V bias) the laser is allowed to go through the “through port”. A varying external electric field thus modulates the continuous wave laser. The highest modulation speed is decided by the photon life time and the flatness of the spectrum around 1542.61 nm. The photon lifetime decides the delay in the ON-OFF transitions. The variations in the spectrum will selectively pass the spectral components produced by the modulation action and hence introduce ripples in the modulated output. The ripples in the spectrum is quantified using a parameter called “signal-Q” [12]. Another performance parameter of a modulator is its extinction ratio (ER). This defines the maximum modulation contrast that can be achieved during modulation. The reduction in Q and ER influences the bit error rate of a system using this modulator. The use of an embedded ring with a sharp roll off of the spectrum and improved flatness [7] of the stop band, helps in increasing both Q and ER as compared to that of single rings of similar dimensions.

The obtained modulation response, shown in Figure 3, has a modulation speed of 20 Gbps for a peak wavelength shift of ~75 GHz at a 7 V drive voltage. At 20 Gbps, the extinction ratio and the signal Q are 12.7 dB and 16 dB, respectively. At 40 Gbps, the extinction ratio of 12 dB is still acceptable with the signal Q deteriorating to 13.4 dB. For similar ring radius of 5 μm , this extinction ratio is much better than those obtained by free carrier tuning [13], whereas the ripple content is similar. At 60 Gbps, although the ER may still be acceptable, the ripple factor becomes a major constraint as $Q < 15.6$ dB is not suitable for dense wavelength division multiplexing (DWDM).

All Optical Switch

Intensity dependent refractive index

The measured intensity dependent refractive index, n_2 , and intensity dependent absorption coefficient α_2 in InGaAsP MQW waveguides, available in the literature [14,15] is adopted here. The nonlinear refractive index in QWs depend mainly on four factors (i) energy of photon (ii) detuning from absorption peak of the QW [14,16] (iii) the optical power level at which the device is operated and (iv) pulse rate of the signal. The MQW heterostructure considered here

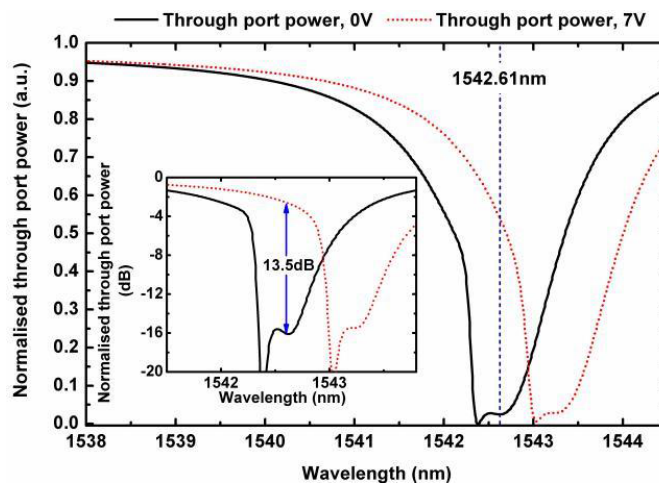


Figure 2: Embedded ring resonator spectrum and tuning for 5 μm outer, 4.45 μm inner ring radii and 2.1 μm straight waveguide segments in outer ring.

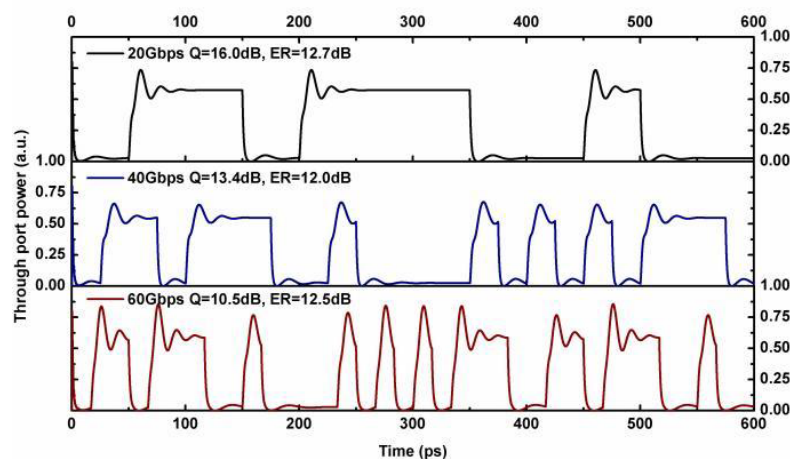


Figure 3: A 5 μm radius embedded ring's 'through port' modulation response, signal Q and extinction ratio (ER) at 20, 40 and 60 Gbps.

has [7] $n_2 = -3.82 \times 10^{-12} \text{ cm}^2/\text{W}$ for a 107 meV detuning and $n_2 = -6.16 \times 10^{-12} \text{ cm}^2/\text{W}$ for a 77 meV detuning [14] whereas the two photon absorption (TPA) coefficient β_2 given as $\alpha_2 = \beta_2 I$ is taken to be 60 cmGW^{-1} , where I is the optical intensity for both the cases [14].

Modeling of all optical embedded ring

The steady state and nonlinear switching models are based on refs. [17,18]. The calculations are performed for input core powers of 1 mW to 1 W. Increments in power are at the rate of 1 mW/ps. An expanded view of the spectrum at resonance is shown in Figure 4. It shows a 0.05 nm shift in the spectrum at a 20 mW input waveguide core power, for a 107 meV detuning of the operating wavelength from the MQW band edge. At low powers of <2 mW (<28 MW/cm² peak intensity in the inner ring core) most of the optical power reaches the, through port. On the contrary, for high peak input core powers of >20 mW (>210 MW/cm² peak intensity in the inner ring core) the spectrum shifts and the output power switches to the ‘drop port’.

Temporal response of nonlinear rings is obtained using finite differencing of nonlinear propagation equation [19] or coupled delayed equations [20]. Coupled delayed equations consider cavities as lumped elements with a life time [21], and are not suitable for nonlinear embedded rings with complex phase distribution in different arms. Here, a slowly varying nonlinear propagation equation has been used [19,22,23]. A complex envelope A_u , written as a function of axial position and time, can be normalized such that $|A_u|^2$ is the axial power flow in a given cross section of the waveguide’s MQW core. The propagation equation for A_u undergoing optical Kerr nonlinearity and two photon absorption (TPA) can be written as [19,22,23]

$$\beta_1 \frac{\partial A_u(z,t)}{\partial t} + \frac{\partial A_u(z,t)}{\partial z} = -j[\gamma_{core} - k_0 n_0(z)]A_u(z,t) \quad (3)$$

where the β_1 is the reciprocal of group velocity, with the low-power propagation constant $e^{-jLk_0 n_0}$ included in the coupling coefficient at the end of each arm of length L_r . The nonlinear complex propagation constant then is given as

$$\gamma_{core} = \beta_{core} - j\alpha_{core} = k_0 \left\{ n_0 + \Gamma n_2 \frac{A_u^2}{A_c} + \Gamma n_{fc} \right\} - j \left\{ \frac{\alpha_0}{2} + \Gamma \frac{\alpha_2 A_u^2}{2 A_c} + \Gamma \frac{\alpha_{fc}}{2} \right\} \quad (4)$$

Here k_0 is the free space propagation constant, and α_0 and n_0 are the low power, loss coefficient and effective index of the waveguide, respectively; n_2 is fast intensity dependent refractive index due to stark effect [14], dominant at low intensities; α_2 is the intensity dependent absorption coefficient giving rise to free carrier effects, dominant at higher intensities; Γ is the mode confinement factor in the core, and Δn_{fc} and $\Delta \alpha_{fc}$ are the bulk refractive index and the absorption coefficient change, respectively, caused by free carriers; A_c is the core waveguide cross section; (3) has been iteratively solved using state machine model [7]. The free carrier concentration (N_{fc}) evolution is given by

$$\frac{dN_{fc}(z,t)}{dt} = \left[\frac{\alpha_2 |A_u|^4}{2\hbar\omega A_c^2} - \frac{N_{fc}(z,t)}{\tau_{total}} \right] \quad (5)$$

Lifetime and τ_{tr} is the carrier transit time including $\tau_{tr} = W^2/V$ and MQW carrier capture time the thickness of the intrinsic region, μ is the mobility and V is the depletion region voltage. The carrier escape times from QW are calculated using [24]. The tunneling time for n^{th} transition in i^{th} band is given by

$$(\tau_T)_{i,n} = \frac{2L_w^2 m_i}{n\hbar\pi} \exp \left[\frac{2L_b \sqrt{2m_{bi} H_i(F)}}{\hbar} \right] \quad (6)$$

Where L_w and L_b are the well and barrier widths respectively, and m_i and m_{bi} are the electron effective masses of the well and the barrier respectively. $H_i(F)$ is the lowered barrier height from i^{th} QW level with the externally applied field F , obtained from the energy band profile. The thermionic emission time is given by

$$\tau_e = \sqrt{\frac{2\pi m_i L_w^2}{kT}} \exp \left[\frac{H_i(F)}{kT} \right] \quad (7)$$

An estimate of the surface recombination lifetime (τ_s) has been obtained using [25]. The effect of screening is considered to be captured by α_2 and the carrier lifetime (τ_{total}) at room temperature; for a large detuning from band edge (>100 meV). The vertical movement of carriers by diffusion is small compared to drift under external field and is hence ignored. Details of electrical contacts for applying external bias at high modulating frequencies have already been discussed in the previous section.

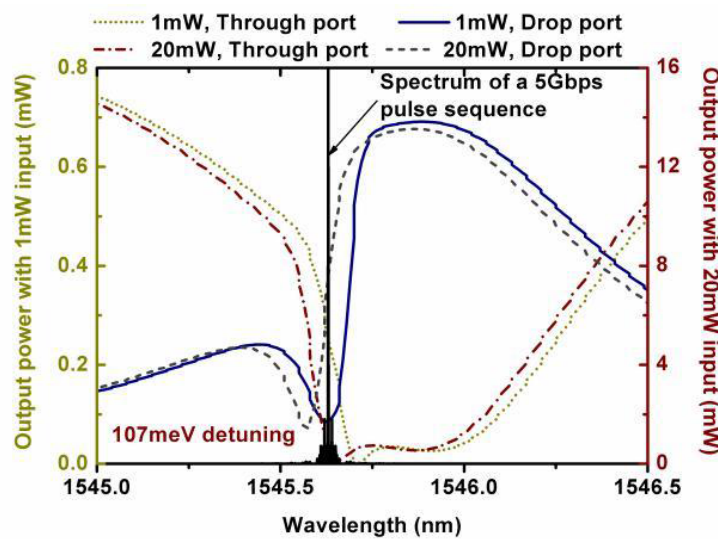


Figure 4: Nonlinear shift in the spectrum of embedded ring resonator with 20 mW input core power. The spectrum of 5 Gbps pulse sequence is also shown. The operation wavelength is 107 meV from QW absorption peak.

The path switching operation

The simulation steps used here for path switching of an input pulse train are $\Delta t=5.28$ fs for time steps and $\Delta z z=0.495$ μm as spatial steps along the length of the waveguides. Additionally, $\tau_{fc}=150$ ps, $\mu=200$ cm^2/Vs , $W=482$ nm, built in potential of -1V, and the input pulse rise and fall times of 1 ps each have been used for the simulation. For a completely undoped layer structure, the built-in potential would be negligible and the carrier life time of 150 ps would be the dominant life time. With a PIN structure, transit times have been obtained using (6, 7) as 12ps for no bias and 2ps for a -7V bias, and hence the calculated τ_{total} have been 15ps and 4ps, respectively. InGaAsP has low surface recombination velocity [26] and an estimate of the surface recombination lifetime ' τ_s ' [27] has been obtained as ~ 1.5 ns, which can be neglected as $\eta_{is} \gg \tau_{total}$.

As described above, the OFF state core pulse power of 2 mW leads to higher output power in the "drop port", and the ON state input core pulse power of 20 mW makes the 'through port' power larger. This path switching process can be used to do various signal processing tasks and optical packet switching as described here with the aid of an optical amplifier, whose gain is controlled by an 'add/drop' signal [28].

Here also, the signal Q is used to quantify ripples in the optical output. The 'switching ratio' defined as

$$\mathfrak{R} = 10 \log \left[\frac{P_{drop,20mW}}{P_{through,20mW}} \right] - 10 \log \left[\frac{P_{drop,2mW}}{P_{through,2mW}} \right] \quad (8)$$

is calculated from Figure 5, where ($P_{i,p}$) is the average power in port 'T' when the input power is 'p'. This parameter is a measure of the maximum nonlinear switching contrast achieved between the two ports.

The field enhancement (FE) which is the ratio of electric field amplitude inside the ring to that at the input waveguide obtained from time domain simulation has been ~ 4 for the inner ring and ~ 2.5 for the outer ring at the required operating wavelength (varies also with power). The large FE of the inner ring, along with electromagnetically

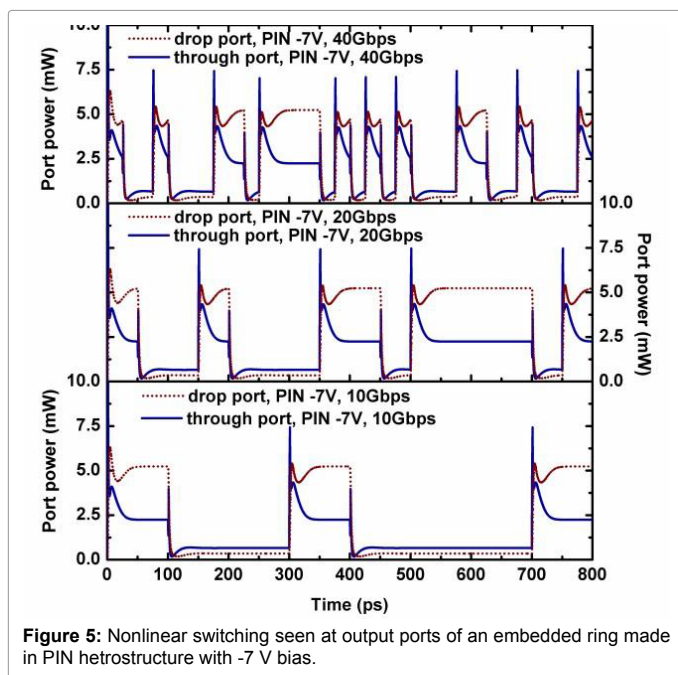


Figure 5: Nonlinear switching seen at output ports of an embedded ring made in PIN hetrostructure with -7 V bias.

induced transparency (EIT) like spectrum helps in obtaining switching at lower input powers, as compared to single ring resonators of the same dimensions. The rise/fall times of the output at the "drop port" has been observed to be 3 ps/5 ps and 30 ps/6 ps, for a -7 V bias and 0 V bias of the PIN heterostructure, respectively. For the embedded rings made in the intrinsic heterostructure, the rise time has been 58 ps and fall time has been 22 ps, due to the lingering of TPA generated carriers [29].

To study the worst case scenario, a 20 mW/2 mW (for logical 1/0) sequence has been simulated as input. The bit sequence used here is cyclically repeated '100100011011110101010001'. With this input, the path is switched in every power transition and both transients due to path switching and high bit rate becomes visible in the output as shown in Figure 5. An ER=5 dB is obtained with 17 dB signal Q at 20 Gbps pulse train in a -7 V biased embedded ring. This is a significant improvement over single ring of similar dimensions, giving 20 dB signal Q but only a 0.46 dB extinction ratio. Stable output is observed for the powers below 600 mW using the time domain model discussed here. In order to ensure stability of the model, an upwind discretisation has been used for both carrier concentration and field envelope equations. The calculated spectral shift, using time and frequency domain methods is found to positively match each other. The nonlinear refractive index coefficient grows nearly exponentially [16] in the QW as the detuning from band edge is reduced. Thus, further reduction in power level for nonlinear switching may be possible, but with increased insertion loss for the device. A comparison of the all-optical embedded ring switching performance with other ring all-optical switches is shown in Table 2. The embedded ring is faster and smaller than most of its single ring counterparts, and require smaller switching pulse energy. The low switching energy allows path switching using the signal power itself without needing a separate pump.

The path switching process can be used to perform optical packet switching as depicted in Figure 6, with the aid of an optical amplifier (for demonstration) whose gain is controlled by an add/drop signal. Here, a high amplitude data packet labeled "Ch.-1" is shown to be dropped and a packet labeled add is shown to be added, while the low amplitude packet "Ch.-2" stays in the through port data stream. Figure 7 shows the simulated path switching in embedded ring for 0V bias in the PIN heterostructure, in which a 40Gbps data sequence is switched at 5G packets per second, with each packet consisting of 8 bits [30].

There is a natural steepening of the spectrum towards the blue edge, caused by resonant wavelengths experiencing stronger field and nonlinearity compared to the non-resonant ones. This steepening has been exploited by using the overlap of resonances on the blue side of the outer ring peak. At lower powers, the free carrier limited nonlinearity

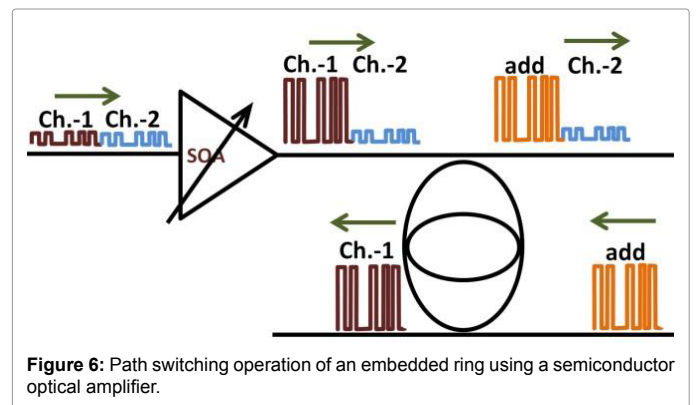
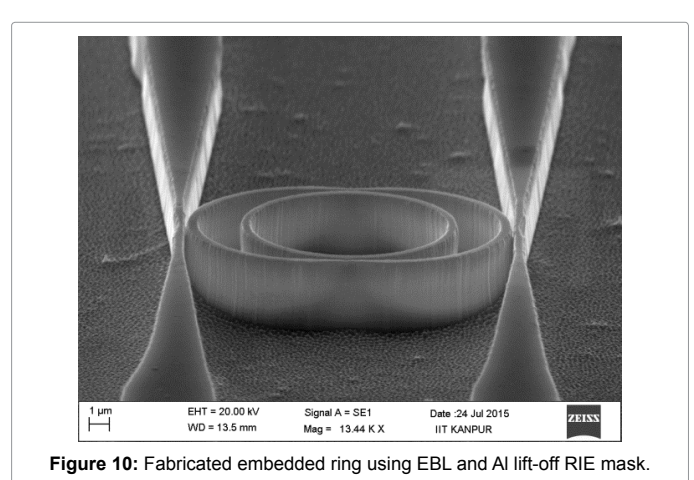
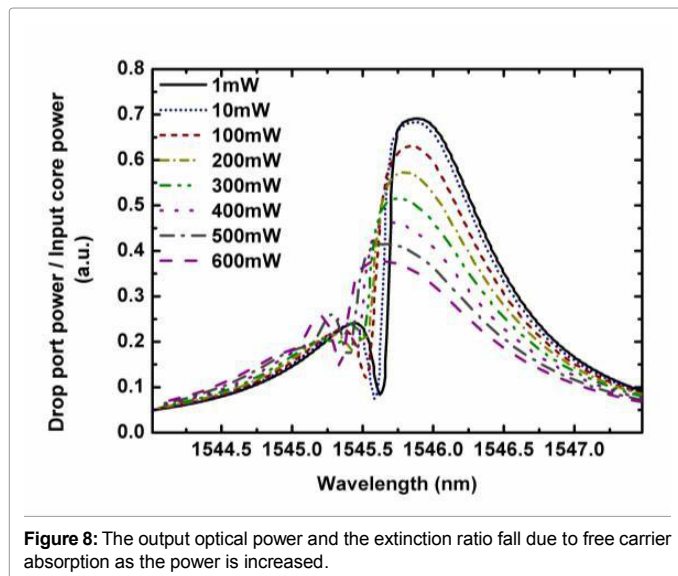
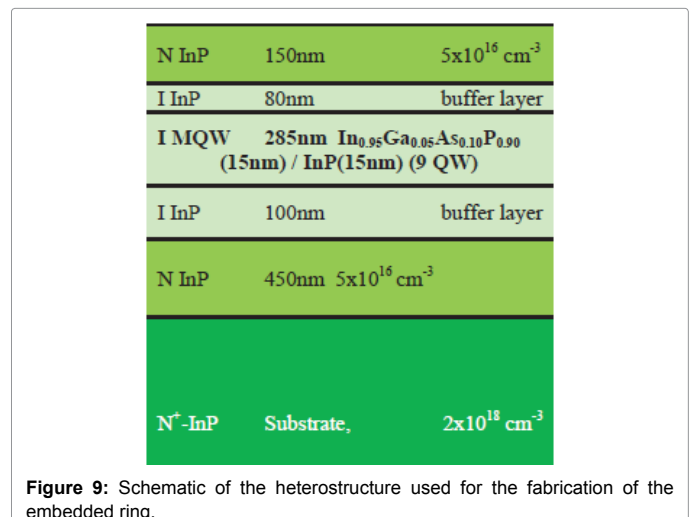
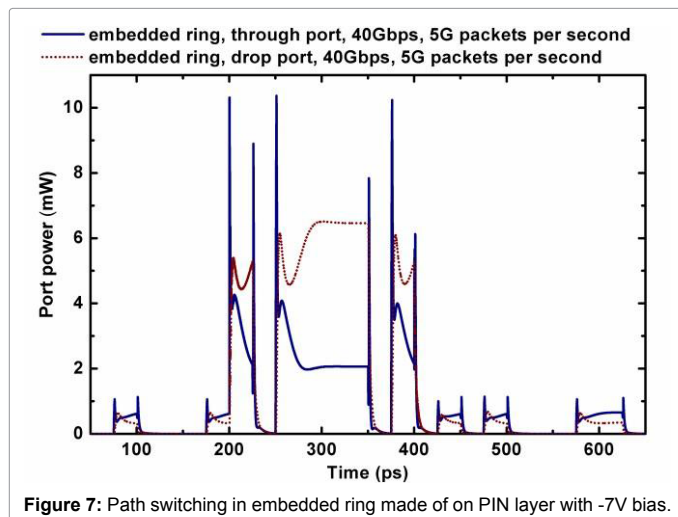


Figure 6: Path switching operation of an embedded ring using a semiconductor optical amplifier.

Reference	Switching time (ps)	ER/R (dB)	Pulse energy (pJ)	Type (year)	area (μm^2)
Van [28]	100	~6	50	GaAs, passive, pump-probe, ring ('02)	~400
Almeida [29]	500	-	25	Si, passive, pump-probe, ring ('04)	100
Hill [30]	20	8-10	.0055	InP, ring laser, memory, coupled ring ('04)	720
Xiong [31]	~50 (10Gbps)	1.2	0.350	Si, four wave mixing, AND gate, ring('13)	9100
This work	4	5	1	InP, reverse biased pin, self-switch, ring	~130

Table 2: Comparison of embedded ring all-optical switch with other reported devices.



is weak and the responses are inherently faster. Additionally, sharpness and the extinction ratio of the spectrum are reduced at higher powers, as shown in Figure 8, due to the increased free carrier absorption.

Fabrication of a Passive Embedded Ring

Embedded rings with and without tapers have also been fabricated in the heterostructure shown in Figure 9 with a MQW band gap of 976 nm. The ring fabrication process using electron beam lithography (EBL) on PMMA 950k/996k bi-layer resist, Al mask lift-off and RIE etching has been reported earlier [31]. The recipe with no O_2 cleaning allowed deep etching and provided a mild profile bowing, which increases the isolation between substrate and the waveguide core regions. A device fabricated by this method is shown in Figure 10. The ridges are $\sim 4.5 \mu\text{m}$

tall and, the bus waveguide is $4 \mu\text{m}$ wide and $225 \mu\text{m}$ long (input port to through port). The ring has a 450 nm to $\sim 200 \text{ nm}$ optical taper in the coupling region, with a $5 \mu\text{m}$ outer and a $4.45 \mu\text{m}$ inner ring radii. The bent waveguides are 500 nm wide. The coupling gap has been $\sim 100 \text{ nm}$ in QW core region which widens to $\sim 250 \text{ nm}$ at the upper cladding region due to mask erosion.

The measured spectrum has been obtained after antireflection (AR) coating of the input facets. From a theoretical fit to this spectrum, as shown in Figure 11, the effective indices are obtained as 2.96 in straight and 2.87 in bent waveguides. A bent waveguide loss of 400dB/cm has also been measured. This measured embedded resonance has strong resemblance between the theoretical and the experimental data. The resonance linewidth measured here is $\sim 6 \text{ nm}$ and is significantly broader due to larger waveguide losses. Hence high speed modulation experiments could not be performed, for which a $\sim 1 \text{ nm}$ linewidth is more meaningful.

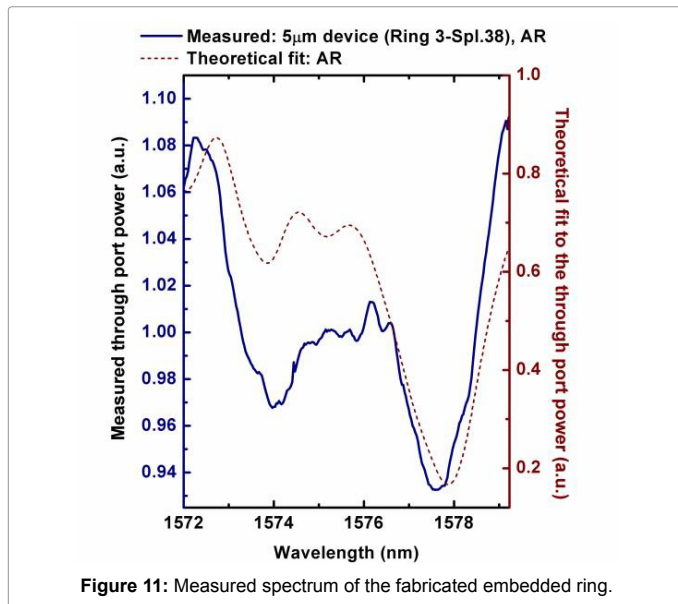


Figure 11: Measured spectrum of the fabricated embedded ring.

Acknowledgement

The epitaxial InGaAsP MQW heterostructure has been provided by Professor C Jagdish, ANU, Canberra for which we are grateful. Support from Dept. of Physics and Dept. of EE, IIT Kanpur for the use of SEM and EBL equipments are also gratefully acknowledged.

References

- Little BE, Chu ST, Haus HA, Foresi J, Laine JP (1997) Microring Resonator Channel Dropping Filters. *J Light Technol* 15: 998-1005.
- Xu Q, Manipatruni S, Schmidt B, Shakya J, Lipson M (2007) 12.5 Gbit/s carrier-injection-based silicon micro-ring silicon modulators. *Opt Express* 15: 430-436.
- Ibrahim TA, Grover R, Kuo LC, Kanakaraju S, Calhoun LC, et al. (2003) All-optical switching using a critically coupled InP micro-racetrack resonator. *Integ Photo Res, Washington DC, USA* 91: ITuE4.
- Zhang L, Song M, Wu T, Zou L, Beausoleil RG, et al. (2008) Embedded ring resonators for microphotonic applications. *Opt Lett* 33: 1978-1980.
- Nawrocka MS, Liu T, Wang X, Panepucci RR (2006) Tunable silicon microring resonator with wide free spectral range. *Appl Phys Lett* 89: 071110.
- Fetterman M, Chao CP, Forrest SR (1996) Fabrication and Analysis of High-Contrast InGaAsP-InP Mach Zehnder Modulators for Use at 1.55-µm Wavelength. *Photo Tech Lett* 8: 69-71.
- Sadasivan V, Das U (2014) QCSE Tuned Embedded Ring Modulator. *Light Tech J* 32: 107-114.
- Grover R, Ibrahim TA, Kanakaraju S, Lucas L, Calhoun LC, et al. (2004) A tunable GalnAsP-InP optical microring notch filter. *Photo Tech Lett IEEE* 16: 467-469.
- Chen H (2007) Development of an 80 Gbit/s InP-based Mach-Zehnder Modulator. *Tech Univ Berlin*.
- Ding XZ, Tajing L, Ong CK, Tan BTG (1994) Effects of impurity concentration on dielectric loss in Zn-doped InP at microwave X-band frequencies. *J Appl Phys* 75: 7444-7447.
- Krupka J, Hartnett JG, Piersa M (2011) Permittivity and microwave absorption of semi-insulating InP at microwave frequencies. *Appl Phys Lett* 98: 112112.
- Agrawal GP (2002) *Fiber-Optic Communication Systems* (3rd edn) John Wiley and Sons, New York.
- Zhang L, Song M, Beausoleil RG, Willner AE (2009) A High-Speed Silicon Modulator Based on an Embedded-Ring-Resonator Structure. *OSA publish*, pp: 22-26.
- Seo JK (2006) Study of time-resolved measurement of intensity-dependent refractive index change in GalnAsP waveguides. *Tokyo Inst Tech*.
- Hall KL, Darwish AM, Ippen EP, Koren U, Raybon G (1993) Femtosecond index nonlinearities in InGaAsP optical amplifiers. *Appl Phys Lett* 62: 1320-1322.
- Ehrlich JE, Neilson DT, Walker AC, Hopkinson M (1993) Guided-wave measurements of real-excitation optical nonlinearities in a tensile strained InGaAs on InP quantum well at 1.5 µm. *Opt Commun* 102: 473-477.
- Sadasivan V, Das U (2014) Optical switching in InGaAsP/InP Embedded Ring Resonators. *Inter Conf Fibre Optic Photo M4A* 30: 13-16.
- Viswas S Nair (2017) InGaAsP/InP multi-quantum well embedded ring Electro-optic or All-optical modulators, filters and switches. *IIT Kanpur, India*.
- Van V, Ibrahim TA, Absil PP, Johnson FG, Grover R (2002) Optical signal processing using nonlinear semiconductor microring resonators. *Sel Top Quant Elect IEEE J* 8: 705-713.
- Eksioglu Y, Petracek J (2014) Self-pulsing and chaos in Kerr-nonlinear coupled ring resonators. *ICTON 16th Inter Conf Graz, Austria*, pp: 1-4.
- Little BE, Chu ST, Haus HA, Foresi J, Laine JP (1997) Microring resonator channel dropping filters. *Light Tech J* 15: 998-1005.
- Okamoto K (2006) *Fundamentals of Optical Waveguides*. (2nd edn.) Academic Press.
- Hsieh IW, Xiaogang C, Dadap IJ, Panoiu NC, Osgood RM, et al. (2006) Ultrafast-pulse self-phase modulation and third-order dispersion in Si photonic wire-waveguides. *Opt Express* 14: 12380-12387.
- Fox AM, Miller DAB, Livescu G, Cunningham JE, Jan WY (1991) Quantum well carrier sweep out: relation to electroabsorption and exciton saturation. *Quantum Electron IEEE J* 27: 2281-2295.
- Sprout AB (1994) Dimensionless solution of the equation describing the effect of surface recombination on carrier decay in semiconductors. *J Appl Phys* 76: 2851-2854.
- Sakai S, Umeno M, Amemiya Y (1980) Measurement of Diffusion Coefficient and Surface Recombination Velocity for p-InGaAsP Grown on InP. *Jpn J Appl Phys* 19: 109.
- Van V, Ibrahim TA, Absil PP, Johnson FG, Grover R, et al. (2002) Optical signal processing using nonlinear semiconductor microring resonators. *Sel Top Quantum Electron IEEE J* 8: 705-713.
- Almeida VR, Barrios CA, Panepucci RR, Lipson M (2004) All-optical control of light on a silicon chip. *Nature* 431: 1081-1084.
- Hill MT, Dorren HJS, de Vries T, Leijtens JMX, den Besten JH, et al. (2004) A fast low-power optical memory based on coupled micro-ring lasers. *Nature* 432: 206-209.
- Xiong M, Lei L, Ding Y, Huang B, Ouet H, et al. (2013) All-optical 10 Gb/s AND logic gate in a silicon microring resonator. *Opt Express* 21: 25772-25779.
- Sadasivan UDV (2015) Fabrication of low grass, smooth sidewall InGaAsP by Methane-Hydrogen ICP RIE through a metal lift-off mask patterned by e-beam lithography. *J Vac Sci Tech B* vol: 33.